ACS Catalysis

Research Article

pubs.acs.org/acscatalysis

First-Principles Analysis of Structure Sensitivity in NO Oxidation on Pt

J. M. Bray and W. F. Schneider*

Department of Chemical and Biomolecular Engineering, 182 Fitzpatrick Hall, University of Notre Dame, Notre Dame, Indiana 46556, United States

Supporting Information

ABSTRACT: The kinetics of Pt-catalyzed NO oxidation on both Pt(111) and Pt(321) are quantified from first-principles using a coverage-aware "reaction site" kinetic model. Density functional theory (DFT)-parametrized cluster expansions are used to predict oxygen coverages and availability of O_2 dissociation sites as a function of reaction conditions. DFT calculations are used to parametrize a Brønsted−Evans−Polanyi relationship for O_2 dissociation on Pt(321). Ensemble averaging over available sites and their corresponding rates yields total reaction rates. Predicted apparent activation energies and rate orders are consistent with the experimental observations on single crystal catalysts and are most strongly determined by the coverage dependence of O adsorption rather than the statistical availability of O_2 dissociation sites. Rates and rate derivatives are similar on the two surfaces over the range of experimental observation and are predicted to differ more significantly outside this range.

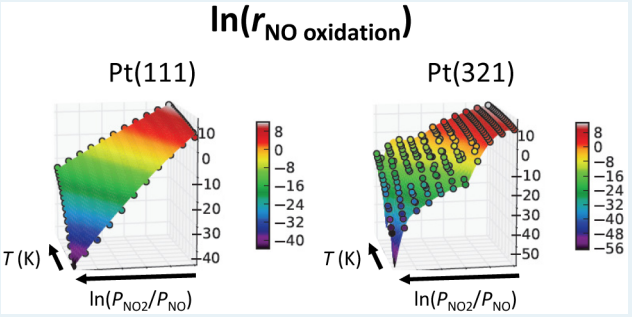

KEYWORDS: *NO oxidation, structure sensitivity, Pt catalyst, first-principles kinetics, DFT, cluster expansion*

1. INTRODUCTION

NO oxidation to NO_2 is a key component in a number of NO_x remediation technologies,[1,2] including NO_x storage and reduction,[3,4] selective catalytic reduction,[5−7] and the continuously regenerating trap.[8] Platinum is the most common catalyst used in these mobile source applications, in which both catalyst activity and durability are key considerations.

NO oxidation rates have been measured on supported Pt nanoparticles as well as on single-crystal Pt surfaces.[2,9−14] Mulla et al. and Weiss et al. observed that NO oxidation turnover rates increased with increasing particle size.[9,11] This type of supported particle size effect could reflect a kinetic structure sensitivity, in which smooth, flat terraces that dominate larger particles react at a different rate from rough, jagged edges and corners. Alternatively, factors such as the intrinsic resistance of a catalytic particle to deactivation could manifest itself as a structure sensitivity.[15] These experimental observations prompted investigation of single crystal model catalysts to directly probe NO oxidation structure sensitivity and reveal the cause of the structure effect.

Smeltz et al. reported NO oxidation rate measurements over single crystals of Pt(111), chosen to model the terraces of large particles; and Pt(321), chosen to model nanoscale particles. The (321) facet exposes five unique surface Pt that organize to form steps, kinks, and close-packed terraces.[16] The 1:1:3 ratio of step/kink/terrace atoms is similar to that of 2−3 nm Pt nanoparticles (assuming a cuboctahedron structure),[14,17] thereby making it a useful model for the edge and corner defect sites on nanoparticles of that size. Smeltz et al. found that absolute turnover rates were approximately the same in each case, to within a factor of 2.[14] In addition, the rate orders and apparent activation energies were also very similar for the two systems. This single crystal structure insensitivity is both surprising and clearly not an explanation for the observed particle size effects.

The NO oxidation mechanism itself and its transferability from surfaces to nanoparticles remains unresolved. In particular, analysis of experimental observations on nanoparticles can be interpreted in terms of a model in which O_2 adsorbs molecularly prior to dissociation and this molecular adsorption step is rate-limiting.[2,11,14] Getman et al. combined density functional theory (DFT) computation and experiment to infer that atomic O is the primary surface species present during NO oxidation.[10,12] Furthermore, calculations indicate that both O adsorption and O_2 dissociation are coverage-dependent, features that must be captured in any mean-field microkinetic model.[12,18] These repulsive lateral interactions are important in partially passivating the metal surface, weakening O binding sufficiently to make the catalyst surface active for the oxidation of NO to NO_2. These interactions are also found to increase the O_2 dissociation barrier in accordance with expectation from a Brønsted−Evans−Polanyi (BEP)-type relationship between final state binding and transition state activation energies.[19−22] These effects are

Received: November 10, 2014
Revised: December 26, 2014
Published: December 30, 2014

DOI: 10.1021/cs501783q
ACS Catal. 2015, 5, 1087−1099

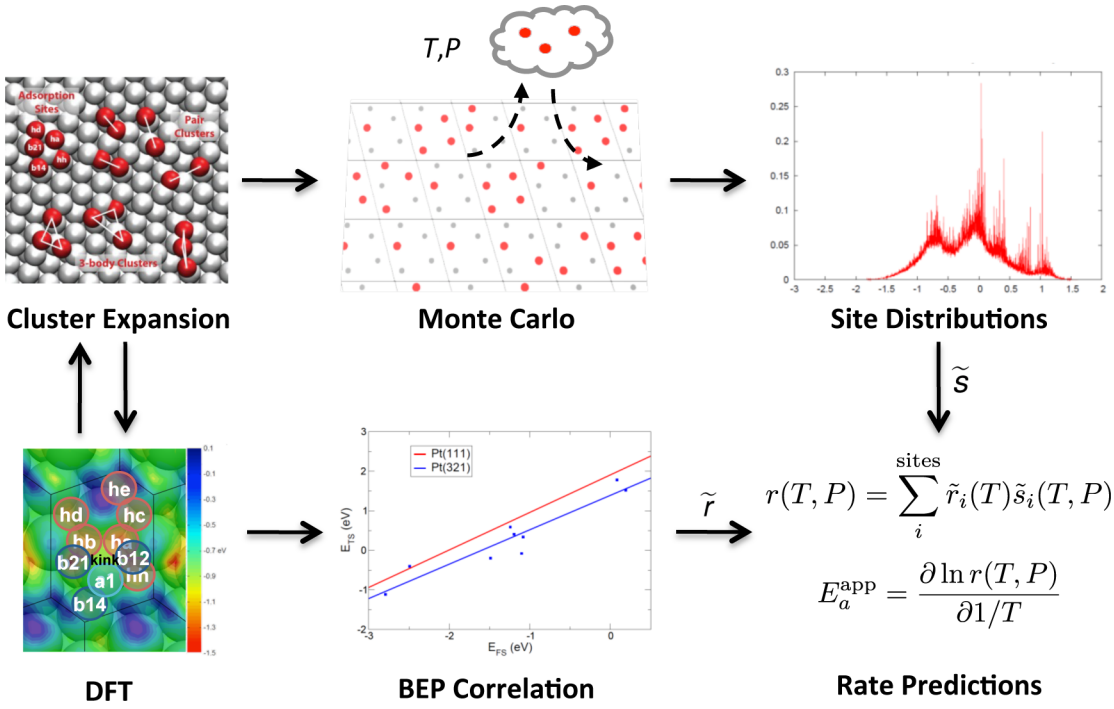

Figure 1. Summary of the reaction site model implementation for NO oxidation rate predictions. Site densities, $\tilde{s}$, are obtained from CE/GCMC simulation, whereas site-specific rates, $\tilde{r}$, are determined from the BEP relationship.

predicted to combine to make O_2 dissociation rate-limiting.[12,23] Assuming a linear dependence of both binding and activation energies on coverage, Getman et al. were able to reproduce many of the key trends and behaviors of the experimental system.[23]

Mei et al.[15,24] and Ovesson et al.[25] reported the first lattice-based Monte Carlo simulations of NO oxidation on Pt(111), incorporating approximate descriptions of the adsorbate–adsorbate interactions and noting the sensitivity of the catalysis to oxygen coverage. More recently, Schmidt et al. proposed a lattice-based cluster expansion (CE) model to improve predictions of O coverage dependence.[26] Wu et al. combined the CE with grand canonical Monte Carlo (GCMC) simulations and a BEP assumption for O_2 dissociation to model NO oxidation over Pt(111).[27] This model reproduced observed rate orders and apparent activation energies with good reliability. Nielsen et al. have since provided independent confirmation of these findings applying kinetic Monte Carlo to the full reaction mechanism with no rate-determining step assumption.[28]

In this work, we apply the same "reaction site" approach introduced by Wu et al.[27] to compare first-principles-predicted NO oxidation rates on Pt(111) and Pt(321). We adopt the same minimal kinetic model in which NO oxidation to NO_2 is rapid, O_2 dissociation is rate-limiting, and O is the most abundant surface intermediate:[12,27,29]

$$\mathrm{NO(g)} + \mathrm{O^*} \rightleftharpoons \mathrm{NO_2(g)} + * \quad (1)$$

$$\mathrm{O_2(g)} + 2* \overset{\mathrm{rds}}{\rightarrow} 2\mathrm{O^*} \quad (2)$$

Figure 1 summarizes the overall modeling scheme. We draw on previous reports of O adsorption, CE parameters, and O_2 dissociation BEPs on Pt(111).[12,26,27,30,31] The (321) facet introduces additional structural complexity over that of the (111) facet. To deal with this complexity, we use a combination of DFT calculations and the CE technique to both identify adsorption sites on the facet and describe their energetics as a function of overall surface coverage.[32] We use the converged CE results to identify candidate O_2 dissociation sites and configurations, which we then quantify through DFT computation of dissociation transition states and activation energies reported here. These energies are mapped to a BEP that relates final state adsorption energies for reaction 2 to dissociation barriers. Grand canonical Monte Carlo simulations of reaction 1 as a function of temperature and pressure are used to determine the density of O_2 dissociation sites vs reaction conditions. Reaction rates and rate derivatives are obtained by ensemble averaging over sites weighted by the BEP predicted activation energies.

We find that the simple, fully first-principles kinetic model combined with the CE-based coverage-dependence reproduces the structure insensitivity observed in experiments. Computed rates are similar on both surfaces across the range of temperatures and pressures of experimental relevance despite the differences in surface structure, coverage dependence of O adsorption, and O_2 dissociation BEPs. Steady state absorbate coverages are higher on Pt(321) than Pt(111), as also observed. Computed rate derivatives, including apparent sensitivity to oxygen chemical potential, and temperature, also are found to vary in ways consistent with experiments. We decompose the contributions to the rates and derivatives and show that they are dominated by the "site-averaged" activation energy, $\bar{E}_a$, the effective activation energy if all sites were equivalent, rather than the statistical number of available reaction sites.

2. COMPUTATIONAL DETAILS

Density functional theory calculations were performed with the Vienna ab initio simulation package (VASP) version 4.6.[33] The GGA-PW91 exchange correlation functional[34] was used with the projector augmented wave (PAW) frozen core model[35,36] and a plane wave basis set cutoff of 400 eV. Further computational details for the Pt(321) slab model have been reported

DOI: 10.1021/cs501783q
ACS Catal. 2015, 5, 1087–1099

previously.[16,32] O_2 dissociation activation energies on Pt(321) were computed using the climbing-image nudged elastic band (CINEB) method.[37] This approach performs a constrained optimization of several intermediate structures, or images, connecting optimized initial and final states to locate the minimum energy path between them. Once located, vibrational spectra were calculated for all transition states to verify the existence of only one imaginary mode. CINEB calculations were converged for O_2 dissociating on an adsorbate-free Pt(321) surface and in the presence of coadsorbed O in the preferred 0.2 and 0.6 ML ordered arrangements.[32] Several unique pairs of initial O_2^* and final state 2O* configurations were explored at each coverage. When local minima appeared along a minimum energy pathway, these structures were optimized separately, and two new CINEB calculations forked to separately determine the pathway from the initial state to the local minimum and from the local minimum to the final state.

GCMC calculations were performed for oxygen adsorption on a Pt(111) surface using the fcc-only, 12-cluster CE detailed in references 26 and 27 and on the Pt(321) surface using the 5-site, 114-cluster model described in ref 32. A 42 × 42 unit cell lattice was used for both surfaces. The temperature (T) was scanned from 400 to 1200 K in 25 K increments, and O chemical potential (μ_O) varied in 0.1 eV/O increments from −1.9 to 0.8 eV/O. Corresponding O coverages range from a clean surface up to 0.8 and 0.9 ML on Pt(111) and Pt(321), respectively. Two independent simulations were run in parallel for each T/μ_O pair, one starting from an ordered and the other from a random configuration. All surface sites, filled or vacant, were sampled with equal probability. The simulations were considered equilibrated when the normalized histograms of single site energies, tabulated independently for each simulation, differed by <1%. Following equilibration, 10^7 MC steps were taken to accumulate statistics on vacant pair reaction sites associated with each randomly selected surface site, and histograms were normalized to the total number of pair sites sampled.

3. RESULTS

3.1. O_2 Dissociation Pathways on Pt(321). As previously described,[16,32] atomic O binds to Pt(321) in both bridge and 3-fold hollow sites, with the strongest chemisorption occurring at the kink sites. Molecular O_2 also binds most strongly in bridge sites at the step edge and so competes with atomic O for the same binding sites at low coverages. In describing binding sites and dissociation pathways, we follow the site-naming convention introduced previously,[16] summarized in Figure 2.

O_2 is computed to adsorb molecularly and to dissociate with a barrier of ∼0.5 eV (relative to adsorbed O_2) on adsorbate-free Pt(321).[16] Although both O and O_2 adsorption weaken as O coverage increases and preferred binding sites become filled, O_2 dissociation does continue at room temperature up to at least 0.6 ML O.[32,38] We used the preferred ordered oxygen structures at 0.2 and 0.6 ML as models to explore this coverage-dependent O_2 dissociation.

In the 0.2 ML structure, O atoms occupy every b21 site, whereas at 0.6 ML, O fills four additional sites, forming Pt_2O_6 clusters on the surface.[32] Test calculations show that for both coverages, an O_2 molecule prefers to adsorb at the b13 site shown in Figure 2, and we took this as the starting point for all O_2 dissociations reported here. Of the various sites where O adsorbs, only five (ha, hd, hh, b12, b14; see Figure 2d) remain relevant over a wide range of coverage and are incorporated into the Pt(321)−O cluster expansion.[32,39] We similarly restricted our analysis of potential dissociation pathways to these sites.

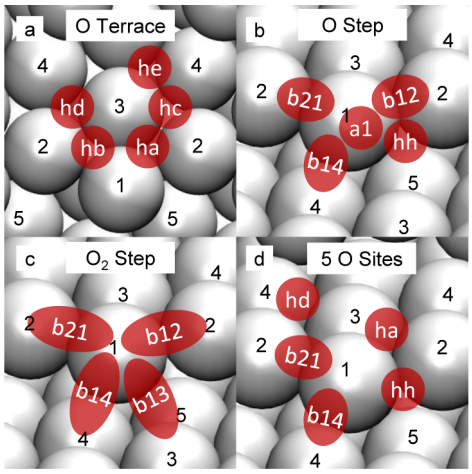

Figure 2. Representative terrace (a) and step (b) atomic oxygen adsorption sites on Pt(321) and step (c) sites for O_2 adsorption. (d) Five sites used in Pt(321)−O cluster expansion and O_2 dissociation pathway development. Atop, bridge, and 3-fold sites are labeled "a," "b," and "h," respectively, and surface Pt numbered 1−5 from the kink atom across the terrace to the step edge.

From the 0.2 ML + O_2 initial state, we considered all possible pairs of O adsorption sites within a nearest neighbor ring proximal to the adsorbed O_2 and that could potentially be reached by a direct dissociation pathway. Of seven such O−O pairs identified, one (b14−hd) was found to be unstable. The six remaining potential final states are represented in Figure 3. For reference, these are identified by combining the labels of the dissociated O atoms, ordered from left to right and top to bottom according to the surface orientation shown in the figure: b14−ha, b14−hh, ha−b14, ha−hh, hh−ha, and hh−hd.

NEB transition state searches were initialized using intermediate structures linearly interpolated between the initial and final states. Five of the six initial attempts encountered local minima, some involving a simple rotation or diffusion of the O_2 molecule and others involving dissociation into sites other than those specified. In these cases, the initial TS searches were split into separate calculations connecting successive minima. Each of the pathways explored was unique, and only select key features of the results are mentioned here. Final results, including transition state energies for the converged pathways, are summarized in Figure 4.

Both pathways b14−hh and hh−ha pass through local minima and converge to transition states typical of an O−O bond dissociation. The imaginary frequencies along the reaction coordinate are in the range 290i to 330i cm^{-1}. The local minimum in the latter case included a single dissociated O in the b13 bridge site. On the clean surface, this site does not adsorb atomic O,[16] yet in the presence of coadsorbed O, the kink Pt exhibits additional mobility, making adsorption in this site possible. The hh−hd and ha−hh O_2 dissociation pathways also exhibited typical transition state characteristics and imaginary mode frequencies similar to those already mentioned. These two pathways passed through local minima containing O adsorbed in the a1 atop site. These atop O intermediates have a characteristic Pt−O stretch frequency around 700 cm^{-1} that is observed in O_2 dosing experiments.[32,38] We have previously shown that this atop O intermediate relaxes to lower energy sites with small barrier.[16]

DOI: 10.1021/cs501783q
ACS Catal. 2015, 5, 1087−1099

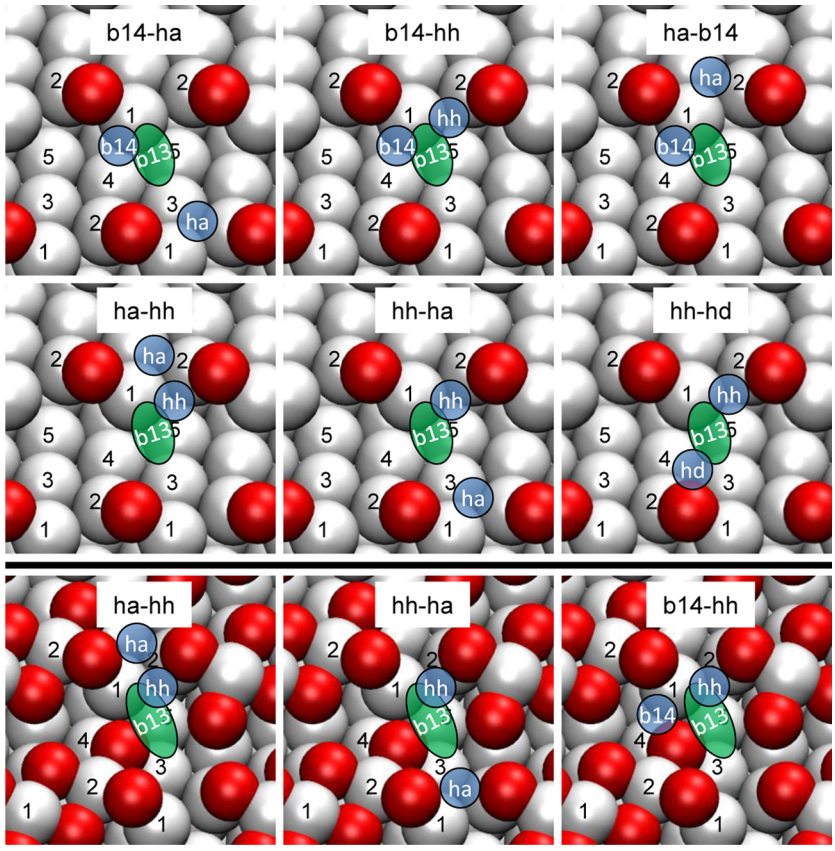

Figure 3. Initial "b13" O_2 adsorption site and O destinations considered on the 0.2 ML (top two rows) and 0.6 ML (bottom row) structures. White = Pt, red = spectator O, green = O_2 initial state, and blue = dissociated O−O final state.

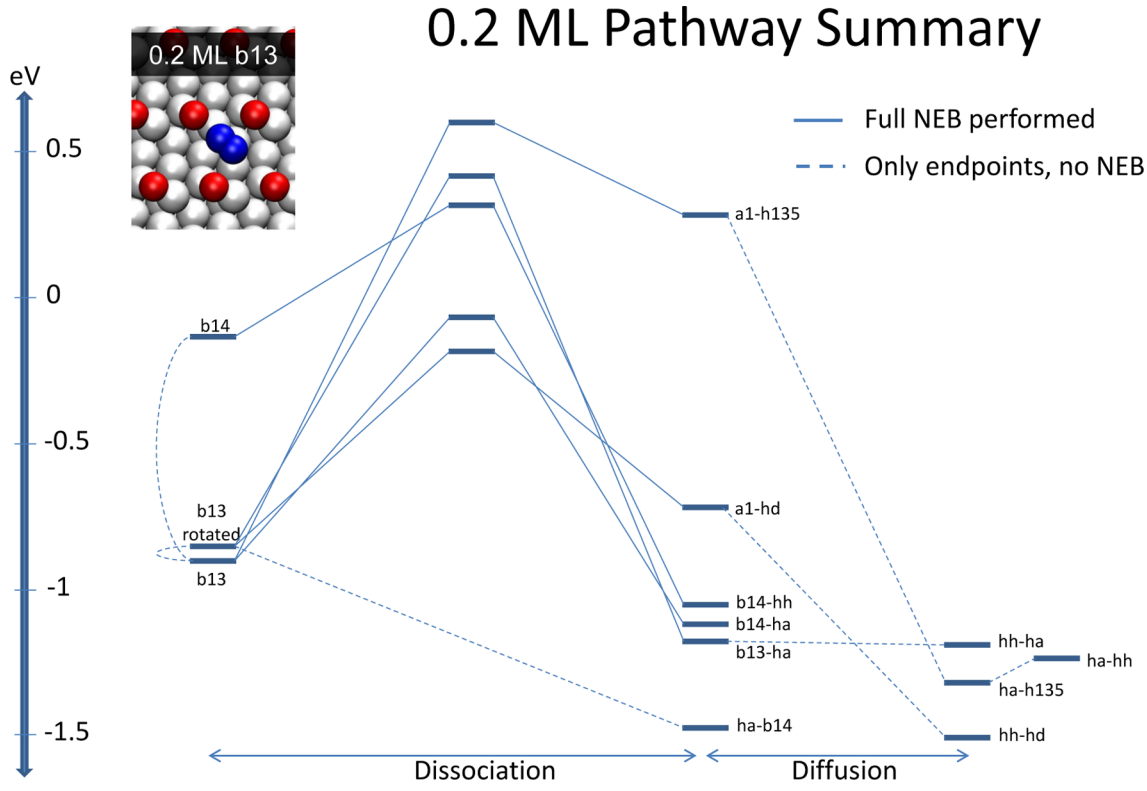

Figure 4. NEB results for O_2 dissociation from the "b13" site at 0.2 ML (inset image, "b13" O_2 in blue). Solid lines indicate fully converged NEB calculations. Dashed lines indicate pathways either not attempted or not converged. All structures provided in Supporting Information.

DOI: 10.1021/cs501783q
ACS Catal. 2015, 5, 1087−1099

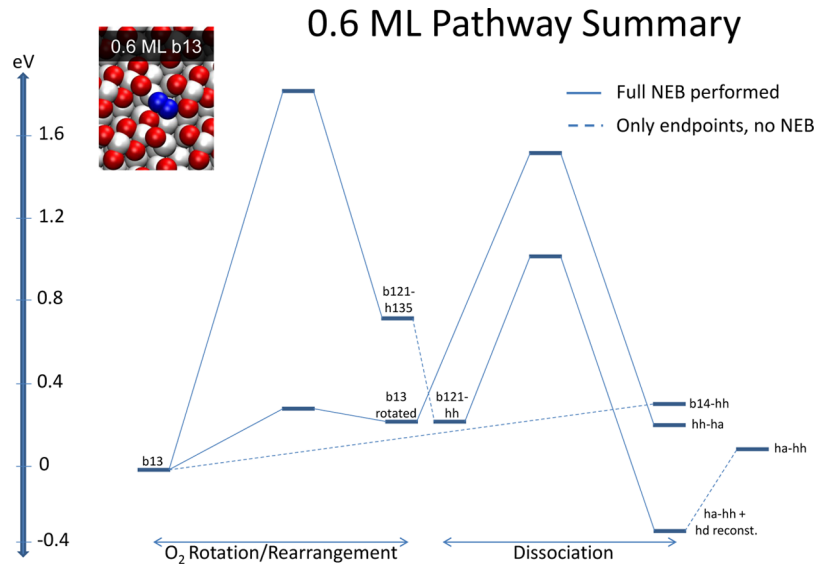

Figure 5. NEB results for O_2 dissociation from the "b13" site at 0.6 ML (inset image, "b13" O_2 in blue). Solid lines indicate fully converged NEB calculations. Dashed lines indicate pathways either not attempted or not converged. All structures provided in Supporting Information.

The b14−ha pathway converged readily and without presenting any local minima. The O−O distance in the transition state was found to be 2.84 Å with a frequency along the reaction coordinate (124i cm^{-1}) atypical of O_2 dissociation (300−400i cm^{-1}). This path corresponds to diffusion of an O adsorbate across a Pt atop site (no. 3 Pt) into the ha hollow. We stopped pursuing the ha−b14 pathway before reaching a converged solution because the intermediate results point toward a similarly low imaginary frequency mode and a pathway again involving diffusion of an O atom over an atop site (no. 1 kink Pt). In these two cases, it appears that the topology of the (321) surface, the presence of coadsorbates, and the choice of final states creates a situation in which O atoms are forced to migrate over unfavorable atop sites such that the diffusion barriers are greater than the actual barrier to dissociation. The impact of coadsorbates is particularly notable in the b14−ha pathway because the no. 3 Pt atop site was shown to be highly unfavorable on the clean Pt(321) surface.[16] Without the influence of the neighboring spectator O atoms, the b14−ha pathway certainly would have avoided this direct atop route in favor of diffusion through bridge and hollow sites.

Fewer O_2 dissociation sites are afforded at the higher, 0.6 ML, coverage. We followed a similar protocol to narrow all possible O−O pairs accessible from the initial b13 O_2. After removing from consideration high energy final states and pathways that were nonviable at lower O coverage, we were left with pathways involving the ha−hh, hh−ha, and b14−hh pairs, illustrated across the bottom of Figure 3. Converged NEB results are summarized in Figure 5, with the initial state structure pictured in the inset. As at lower O coverage, intervening local minima are discovered along the candidate pathways. The hh−ha pathway is simplest and proceeds over a small barrier to a rotated b13 intermediate before crossing a larger dissociation barrier into the final state. This transition state behaves as expected with a dissociation mode frequency near 290i cm^{-1}. The ha−hh pathway evolves in a more complicated fashion: the NEB first discovers a high-energy pathway that scrambles the O_2 oxygens with the nearby b21 O coadsorbate and ultimately places O_2 in a step site with the dissociated O in a hollow site between the nos. 1, 3, and 5 Pt atoms (labeled "b121−h135" in Figure 5; see Supporting Information for image) 0.7 eV above the b13 initial state. There is a 0.5 eV energy benefit for diffusion of the h135 O into the nearby hh site, and an NEB from this b121−hh O2 configuration passes through a TS indicative of single O diffusion (134i cm^{-1} reaction coordinate frequency). The dissociation terminates at a local minimum resembling the designated final state but with the no. 2 Pt on the lower terrace buckling up and the kink Pt relaxing to become 4-fold-coordinated and form a bond with the hd O ("ha−hh + hd reconst." in Figure 5; see Supporting Information for the image). Finally, we were unable to converge a pathway from the O_2 b13 site to the b14−hh final state, likely due to the destabilizing effect of the hd O on the b14 adsorption site. Intermediate results showed both a high barrier and indications of surface reconstruction.

We examined the ability of a BEP to capture the relationship between dissociation and final state energies across this range of pathways. The existence of multiple local minima along the Pt(321) dissociation pathways complicates the selection of transition state−final state pairs for the correlation. Even though some NEB calculations revealed alternative O−O configurations lower in energy than the original final states, we used only the intended final state energy for BEP development. Fitting the BEP to the same set of adsorption sites incorporated into the CE provides a consistent energy reference across all parts of the overall kinetic model. Where the NEB calculations were divided into multiple steps, the highest energy transition state from either elementary step was selected as the transition state of the full, combined pathway.

Figure 6 plots the transition state against the final state energies for the eight available Pt(321) NEB calculations at three oxygen coverages (including two pathways at 0 ML reported previously[16]). A table of all of the converged O_2 dissociation pathways and key energetic parameters associated with each is provided in Supporting Information. The two energies exhibit a positive correlation, as expected, but do have a significant amount of scatter. A linear best fit to the data has a slope of 0.85, intercept of 1.47 eV, and a standard regression error of 0.25 eV and is plotted in Figure 6.

Most of the scatter lies in the intercept. For instance, linear regression on the three pathways having the highest transition

DOI: 10.1021/cs501783q
ACS Catal. 2015, 5, 1087−1099

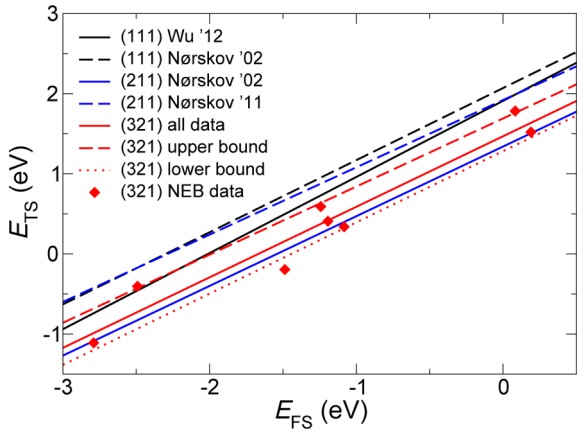

Figure 6. Summary of best-fit O_2 dissociation BEP for Pt(321) as well as several dissociation BEP's reported in the literature. Wu '12 is from ref 27, Nørskov '02 is from ref 21, and Nørskov '11 refers to ref 40.

state energies on the 0, 0.2, and 0.6 ML ground states (pathways 3, 6, and 10 in the table) yields a correlation with a slope of 0.85, intercept of 1.69 eV, and standard regression error of 0.05 eV ("upper bound" in Figure 6). Similarly, the lowest transition state energies at each major ground state (pathways 1, 8, and 9) provide a linear fit (SE = 0.19 eV) with slope of 0.89 and intercept of 1.28 eV ("lower bound" in Figure 6). These correlations compare well with other linear BEP relationships reported in the literature. In particular, Nørskov et al. report a BEP for dissociation reactions of selected diatomics (O_2, NO, N_2, and CO) on (211) stepped surfaces of about a dozen different transition metals to have a slope of 0.87 and an intercept of 1.34 eV.[21,41] A later, more comprehensive study of dissociation reactions (including C−C, C−N, and C−O bond breaking in small organic molecules) suggests a slope of 0.84 and intercept of 1.92 eV.[40] The more positive intercept in this last case can be traced to the choice of the adsorbates at infinite separation as the final state reference. Figure 6 compares our best-fit Pt(321) BEP to these other BEP correlations for stepped surfaces. Despite the different surface structures, metals, and reactant molecules, all correlations occupy a fairly narrow window, again differing primarily in choice of intercept.

Figure 6 also shows two correlations previously reported for dissociation on close-packed surfaces. The first correlation (Wu '12) describes O_2 dissociation on Pt(111) at various surface coverages and is used for the kinetic modeling in this work.[23,27] Compared with the stepped surfaces, this Pt(111) correlation has a steeper slope (1.0) and larger intercept (2.12 eV), indicating transition state energies on the close-packed surface are more sensitive to final state energies. The second correlation (Nørskov '02) is for dissociation of O_2 and other small diatomic molecules across the close-packed surfaces of several transition metals, with a slope of 0.9 and intercept of 2.07 eV.[21]

On both Pt(111) and Pt(321), dissociation pathways exist in which the transition state is lower in energy than the gas-phase O_2 reference. This situation is illustrated in Figure 7a, in which the O_2^* transient intermediate and O* are both strongly bound. As intermediate and final state energies rise, the dissociation transition state rises above the reference energy and becomes positive (Figure 7b). To capture this behavior in the kinetic models below, we use as activation energies

$$E_a = \max[0, E_{TS}] \quad (3)$$

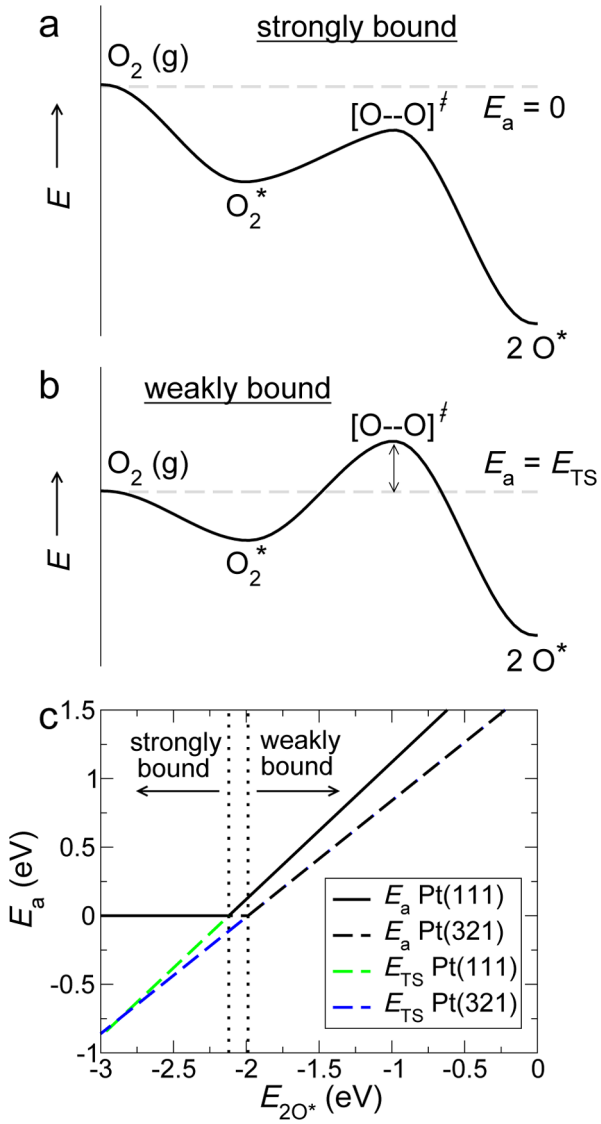

Figure 7. Schematic potential energy diagram for O_2(g) dissociation to 2O*: (a) strongly bound adsorbates characteristic of low coverage; (b) weakly bound adsorbates characteristic of high coverage. (c) O_2 dissociation BEPs on Pt(111) and Pt(321). Dissociations with transition states below the gas-phase reference are assumed to be unactivated.

The BEP for each surface and the resulting activation energies from eq 3 are plotted for comparison in Figure 7c.

3.2. GCMC Results. We used 1-site and 5-site CE's to perform GCMC simulations for O on Pt(111) and Pt(321), respectively, as a function of temperature and chemical potential. Figure 8a shows average O coverage at a representative temperature of 600 K. Key differences between Pt(111) and Pt(321) are evident in the data. The Pt(321)−O system has strong ordering at 0.2, 0.6, and 0.8 ML, evident by the flat regions where coverage changes very little over a wide range of chemical potentials. This strong ordering behavior exists for Pt(111) as well at 0.25 ML, but it disorders at lower temperatures than for Pt(321). Pt(321) generally has a higher equilibrium oxygen coverage than Pt(111) under the same external conditions.

We can use the GCMC results to compute the probability that some randomly selected candidate O_2 dissociation site is vacant. For the (111) surface, we count vacant first-nearest-neighbor fcc site pairs, and for the (321) surface, we count vacancy pairs

DOI: 10.1021/cs501783q
ACS Catal. 2015, 5, 1087−1099

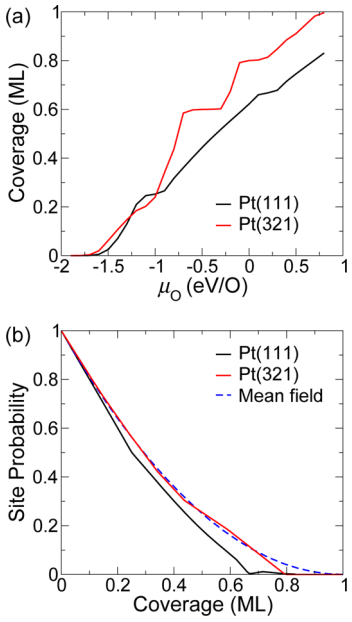

Figure 8. (a) Average coverage vs GCMC chemical potential for Pt(111) (black) and Pt(321) (red) at 600 K. (b) Normalized vacancy pair probability vs average coverage in mean-field (blue) and reaction site models (Pt(111), black; Pt(321), red) at 600 K.

selected to be inclusive of the NEB dissociation pathways described above. Both choices are illustrated in Figure 9.

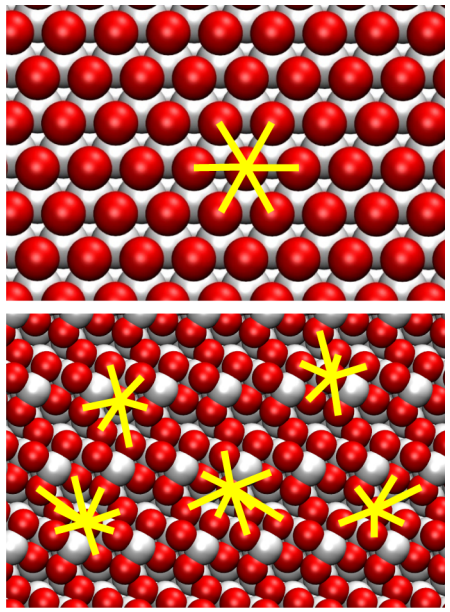

Figure 9. Candidate O_2 dissociation vacancy−vacancy pairs on Pt(111) (top) and Pt(321) (bottom). Pt atoms are white, candidate O adsorption sites are red spheres, and candidate dissociation sites are connected by yellow lines.

Figure 8b reports these candidate reaction site probabilities relative to the probability at 0 coverage ($\sum_i \tilde{s}_i/\tilde{s}_{max}$, as defined in more detail below), plotted vs coverage at 600 K. Probabilities decay linearly at low coverage, more rapidly for Pt(111) than for Pt(321), exhibit kinks near ordered structures, and vanish at the coverages corresponding to ordered structures that offer no vacant sites, at 0.67 ML for Pt(111) and 0.8 ML for Pt(321). These results can be contrasted with the predictions assuming the adsorbates are randomly distributed and uncorrelated. In that case, the probability to select an O_2 dissociation site is the probability to choose a vacant site multiplied by the probability that the partner site is vacant, or $(1-\theta_O)^2$. Figure 8b also reports this mean field expectation vs coverage. The Pt(111) surface offers fewer sites than the mean field prediction at all coverages, reflecting adsorbate−adsorbate repulsions that decrease the likelihood of both occupied−occupied and vacant−vacant neighbor pairs. The deviations become largest at highest coverages. The presence of both attractive and repulsive adsorbate interactions on the Pt(321) surface convolute to make site probabilities agree more closely with mean field expectations until very high coverage.

3.3. Reaction Site Ensemble Averaging. Because of the underlying adsorbate−adsorbate interactions, these aggregated O_2 dissociation sites are not equivalent to one another; rather, they are distinguished by the energy change associated with occupying the site with two O, and through the BEPs of Figure 7c, to the inferred activation energy of O_2 dissociation at the site. Figure 10 reports in black a representative histogram of O_2 dissociation sites on Pt(111), obtained by averaging over the many surface configurations visited in the Monte Carlo, plotted against the corresponding transition state energy. The distribution is smooth and roughly symmetric about the mean.

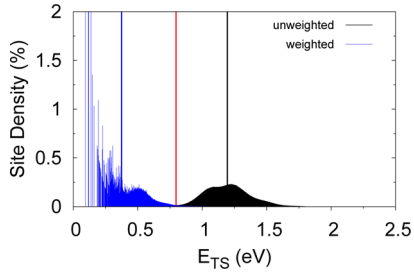

Figure 10. Normalized O−O vacancy pair site distribution on Pt(111) vs transition state energy at T = 600 K and μ_O = −0.7 eV/O, corresponding to θ = 0.361 ML. Raw distribution is in black; Boltzmann-weighted distribution is in blue. Vertical lines indicate average of weighted distribution (blue), site average (red), and statistical mean average (black).

The rate of an O_2 dissociation event, $\tilde{r}_i$, in units $O_2/(s \times$ reaction site) at a site with an activation energy $E_{a,i}$ can be written as

$$\tilde{r}_i(T, P_{O_2}) = A_i(T, P_{O_2}) \exp\left(\frac{-E_{a,i}}{k_B T}\right) \quad (4)$$

Here, P_{O_2} is the oxygen pressure, T is temperature, k_B is the Boltzmann constant, and A_i is the corresponding pre-exponential factor. We make what we call the "reaction site" approximation that all sites of the same $E_{a,i}$ contribute equivalently to a total rate and, thus, that $A_i = A$ for all sites.[27,29] We further write A as the ideal gas flux of O_2 to the surface, linear in P_{O_2}. Exact expressions to deal with the differences in site areas of Pt(111) and Pt(321) are detailed in Supporting Information.

The overall turnover rate ($O_2/(s \times Pt)$) is the sum of $\tilde{r}_i$ weighted by the normalized occurrence of sites of energy E_i, $\tilde{s}_i$, under given external conditions, T and μ_O:

DOI: 10.1021/cs501783q
ACS Catal. 2015, 5, 1087−1099

$$r(T, P_{O_2}, \mu_O) = \sum_{i}^{\text{rxn sites}} \tilde{r}_i(T, P_{O_2}) \frac{\tilde{s}_i(T, \mu_O)}{\alpha \tilde{s}_{max}} \quad (5)$$

Site densities (as in Figure 10) are obtained from GCMC simulations and have units of reaction sites/area. They are normalized to the total number of possible reaction sites on a clean surface of the same area, $\tilde{s}_{max}$. The additional scale factor, α, is the ratio of surface Pt atoms to reaction sites on the clean surface and is required to obtain the desired units. Expanding all terms, α cancels with the area terms in the prefactor, and the model can be reexpressed as

$$r(T, P_{O_2}, \mu_O) = \frac{P_{O_2} A_{Pt}}{\sqrt{2\pi m_{O_2} k_B T}} \sum_{i}^{\text{rxn sites}} \exp\left(\frac{-E_{a,i}}{k_B T}\right) \frac{\tilde{s}_i(T, \mu_O)}{\tilde{s}_{max}} \quad (6)$$

Here, m_{O_2} is the mass of an O_2 molecule, and A_{Pt} is the area of a surface Pt. To highlight the relative kinetic contribution of each site, we plot the argument of the sum, the site distribution weighted by the activation energy, in blue in Figure 10. This distribution is shifted and skewed to the left by the exponential dependence on activation energy; infrequent but lower activation energy sites contribute most significantly to total rates. In this particular case, 99% of the activity is due to only 2.6% of the sites, with activation energies < 0.86 eV. The vertical blue line in the figure indicates the mean of this weighted distribution, which is about 0.4 eV.

The "site-averaged" activation energy, $\bar{E}_a$, is the activation energy that would yield the same total reaction rate if all available dissociation sites contributed equally to the rate. It is closely related to the mean-field apparent activation energy and in general is a function of reaction conditions. It is obtained by averaging the reaction rate over reaction sites:

$$r = \frac{P_{O_2} A_{Pt}}{\sqrt{2\pi m_{O_2} k_B T}} \exp\left(\frac{-\bar{E}_a}{k_B T}\right) \sum_{i}^{\text{rxn sites}} \frac{\tilde{s}_i(T, \mu_O)}{\tilde{s}_{max}} \quad (7)$$

The site-averaged activation energy then follows from eqs 6 and 7:

$$\bar{E}_a = -k_B T \ln\left[\frac{\sum_i^{\text{rxn sites}} \exp\left(\frac{-E_{a,i}}{k_B T}\right) \frac{\tilde{s}_i}{\tilde{s}_{max}}}{\sum_i^{\text{rxn sites}} \frac{\tilde{s}_i}{\tilde{s}_{max}}}\right] \quad (8)$$

The red vertical line around 0.8 eV in Figure 10 indicates $\bar{E}_a$ for the given distribution. Sites with activation energies less than $\bar{E}_a$ account for 98.4% of the total reaction rate in this case.

Figure 11 compares site distributions obtained for the Pt(111) and Pt(321) surfaces under the same conditions. The Pt(321) distributions convolve the contributions of the various physical sites shown in Figure 9 to the overall rate. The site-averaged activation energy is indicated in each case by a vertical red line. Although we see good agreement in the positioning of the red site-averaged activation energy lines, which are an indication of the mean-field observable behavior of the systems, the distributions themselves are quite different. As also seen in Figure 8a, Pt(321) has consistently higher O coverage at the same external conditions, and the distributions themselves have sharper, taller peaks and span a broader range of energies than Pt(111), indicating that Pt(321) is both more ordered and more heterogeneous. As shown below, these differences, when weighted using different BEP correlations and ensemble-averaged over different numbers of available reaction sites, result in similar average properties.

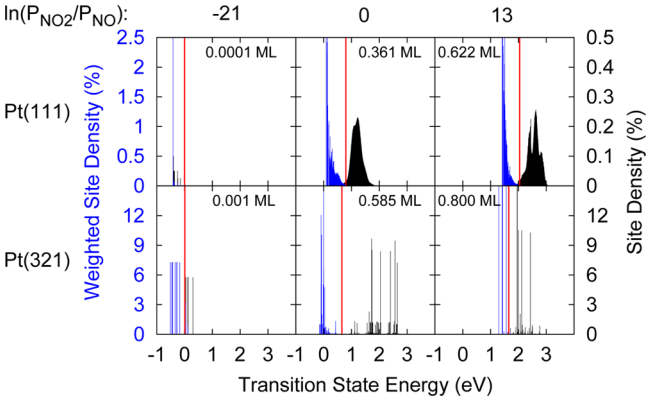

Figure 11. Normalized site distributions for Pt(111) and Pt(321) at 600 K and three chemical potentials spanning low, moderate, and high oxygen coverages. Site-averaged activation energies are indicated by vertical red lines.

3.4. NO Oxidation Rates, Rate Orders, and Apparent Activation Energies. We used eq 6 to compute NO oxidation rates as a function of T and μ_O at 0.1 bar O_2 on both Pt(111) and Pt(321). Under the assumption that the interconversion between NO and NO_2 (reaction 1) is equilibrated, then

$$\mu_{O^*} = \mu_{NO_2} - \mu_{NO}$$

The difference on the right side of the equation is related to P_{NO_2}/P_{NO} through the ideal gas expressions for chemical potentials, as detailed in Supporting Information. There we also relate the chemical potential of surface O, μ_{O^*}, to the GCMC chemical potential, μ_O. These two differ by a temperature-dependent offset. Figure 12 shows the resulting rates on a logarithmic scale vs NO_2/NO ratio for temperatures ranging from 400 to 1200 K. Although differences are apparent at the lower end of this temperature range because of the stronger oxygen ordering tendency on Pt(321), overall, the predicted NO oxidation rates for each surface are nearly identical and have the same general behavior as a function of NO_2/NO ratio.

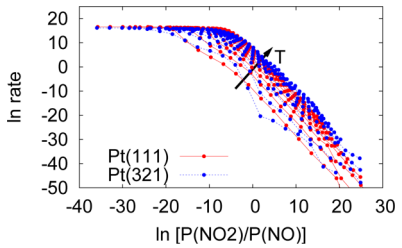

Figure 12. NO oxidation rates on Pt(111) (red) and Pt(321) (blue) as a function of NO_2/NO ratio and temperature at 0.1 bar O_2. Temperature increases from 400 to 1200 K in 100 K intervals.

Smeltz et al.[14] measured NO oxidation rates, apparent rate orders and activation energies over both Pt(111) and Pt(321) as a function of temperature and gas composition. Consistent with the model above, they found rates on the two surfaces to be within a factor of 2. Apparent quantities depended sensitively on reaction conditions. We can extract apparent rate quantities by appropriate differentiation of the data in Figure 12. Smeltz et al. noted that the apparent NO and NO_2 orders were of equal

DOI: 10.1021/cs501783q
ACS Catal. 2015, 5, 1087−1099

magnitude and opposite sign within experimental error, and a similar result follows from the rate model assumptions here.

The NO rate order, then, is the negative slope of the constant temperature lines in Figure 12:

$$n_{NO} = -n_{NO_2} = -\left(\frac{\partial \ln r}{\partial \ln\left(\frac{P_{NO_2}}{P_{NO}}\right)}\right)_{T,P_{O_2}} \quad (9)$$

This slope varies with the NO_2/NO ratio, and resulting NO rate orders for both surfaces are shown in Figure 13 as a function of O

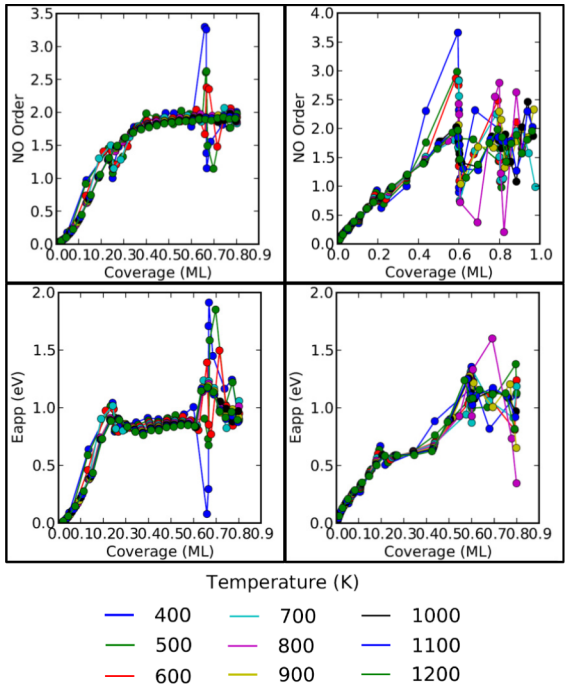

Figure 13. Predicted NO rate orders (top) and apparent activation energies (bottom) for NO oxidation on Pt(111) (left) and Pt(321) (right) as a function of O coverage.

coverage. We find that at low coverages, the rate order is near zero—the rate has no dependence on the pressure ratio—but there is a gradual increase with coverage marked by sharp deviations around the coverages corresponding to the major ordered ground states on each surface. As described in later sections, these deviations are not simulation noise. Rather, they result from changes in the availability of reaction sites due to strong ordering tendencies near ground state coverages. For both surfaces, the rate order eventually plateaus at a value of 2, with the intermediate trend appearing nearly linear with coverage for Pt(321) and less linear for Pt(111).

Figure 14 shows model rate orders plotted side-by-side with the experimental results using identical axes. The experimental data were collected at 573−593 K; we reported results for the closest simulated temperature as well as a higher temperature to probe sensitivity. The range of NO_2/NO ratios shown (from 0.1−1.2) corresponds to O coverages roughly between 0.31 and 0.37 ML on Pt(111) and 0.43 and 0.59 on Pt(321). The model reproduces the similar orders found on the two surfaces as well as the increase from ∼1 to ∼2 with increasing NO_2/NO ratio (and oxygen coverage).

The apparent activation energy is given by

$$E_{app}^{\ddagger} = -k_B\left(\frac{\partial \ln r}{\partial \frac{1}{T}}\right)_{\left(P_{NO_2}/P_{NO}\right),P_{O_2}} \quad (10)$$

GCMC simulations were performed at constant chemical potentials rather than gas pressures, and the necessary conversions are detailed in Supporting Information. The final expression is

$$E_{app}^{\ddagger} = -k_B\left(\frac{\partial \ln r}{\partial \frac{1}{T}}\right)_{\mu_O} + n_{NO}\,\Delta H_{rxn}^{\circ}(T) \quad (11)$$

where the second term includes the standard enthalpy of reaction for the oxidation of NO with surface O (reaction 1). Figure 13 shows the resulting apparent activation energies for NO oxidation on Pt(111) and Pt(321), plotted vs O coverage. At very low coverage, the activation energy is near zero, as expected from the small O_2 dissociation barrier under these conditions. As coverage increases, $E_{app}^{\ddagger}$ increases sharply until the first major ordered ground state is reached (0.25 and 0.2 ML for Pt(111) and Pt(321), respectively). There, it nearly levels off for Pt(111) but continues to increase gradually for Pt(321). As was also noted for the apparent rate order, $E_{app}^{\ddagger}$ includes significant deviations from the overall trend around the major ordered ground states of 0.67 ML for Pt(111) and 0.6 ML for Pt(321). The similarities with the apparent rate order derive from the appearance of the rate order in eq 11.

Figure 14 compares the calculated results with those of Smeltz et al. The simulations reproduce the larger activation energy over Pt(321) than Pt(111), although model-derived results are roughly 20 kJ mol^{-1} greater than observation. Further, the model reproduces the general increase in activation energy observed on Pt(321) with increasing coverage. The apparent activation energy has contributions from the underlying GGA-derived reaction barriers, coverage-dependent binding energies, and the BEP, each of which contributes to the overall error. Considering the simplifications made in the model, the level of agreement is remarkably good.

3.5. Origins of Apparent Kinetic Properties. The rate orders (eq 9) and apparent activation energy (eq 10) can be expressed in terms of the site-averaged activation energy ($\overline{E}_a$, eq 8) by differentiating the rate expression (eq 6). Two terms contribute to the NO order:

$$n_{NO} = \left(\frac{\partial \overline{E}_a}{\partial \mu_O}\right)_T - k_B T\left(\frac{\partial \ln\left(\sum_i^{\text{rxn sites}} \frac{\tilde{s}_i}{\tilde{s}_{max}}\right)}{\partial \mu_O}\right)_T \quad (12)$$

The NO order thus has contributions from the change in $\overline{E}_a$ and change in log total normalized site density, $\sum_i \tilde{s}_i/\tilde{s}_{max}$, with oxygen chemical potential. Figure 15a plots $\overline{E}_a$ and $\sum_i \tilde{s}_i/\tilde{s}_{max}$ vs μ_O at two temperatures for both surfaces. The two terms vary in opposite directions, more smoothly for Pt(111) and with more structure for the more strongly ordering Pt(321). The actual experimental range is a rather narrow band near $\mu_O = -0.7$ eV. The contributions of the two derivatives to n_{NO} are plotted in Figure 15b at 1000 K. Trends are similar at lower temperatures but are obscured by larger fluctuations. It is clear that the site-averaged activation energy—that is, the energy of representative reaction sites—is much more sensitive to μ_O and O coverage than is the density of O_2 dissociation sites. The same idea is

DOI: 10.1021/cs501783q
ACS Catal. 2015, 5, 1087−1099

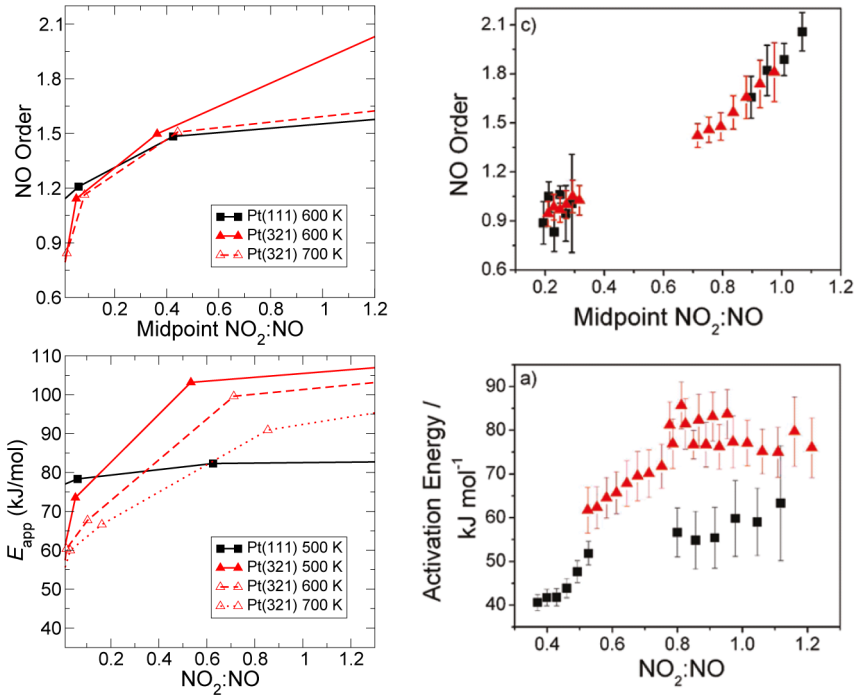

Figure 14. Comparison of predicted NO rate orders and apparent activation energies (left) with experiment (right). Black squares = Pt(111); red triangles = Pt(321). NO orders measured at total NO_x = 120 ppm, T = 573 K for all data except for the Pt(111) data set at large NO_2/NO, where T = 593 K and total NO_x = 90 ppm. Activation energies measured between 473 and 553 K, 76 or 98.8 Torr O_2, and total NO_x of 90−130 ppm, depending on set of data. Midpoint NO_2/NO corresponds to halfway between the minimum and maximum values used to determine the rate order. Experiment adapted from Smeltz et al., *Langmuir* **2010**, 26, 16578−16588 (ref 14). Copyright 2010 American Chemical Society.

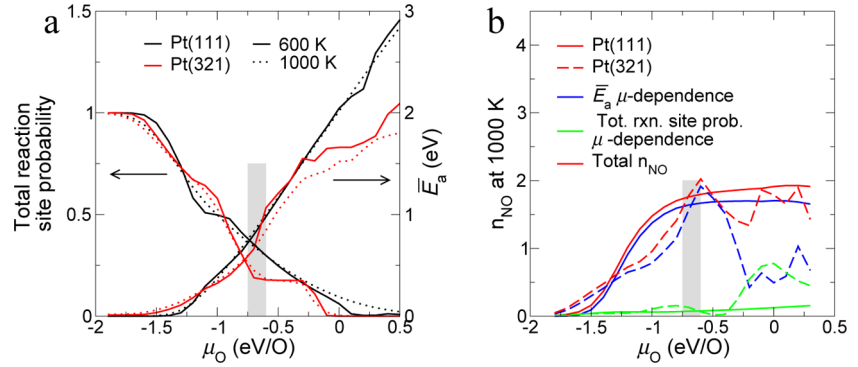

Figure 15. (a) Site-averaged activation energy, $\bar{E}_a$, and total reaction site probability vs simulation chemical potential at 600 and 1000 K. (b) Rate order contributions and total rate order vs simulation chemical potential. Solid lines, Pt(111); dashed lines, Pt(321). Results shown at 1000 K to reduce large fluctuations present at lower temperatures. Gray shaded regions indicate experimental NO oxidation conditions with NO_2/NO ratio ∼ 1.

conveyed in Figure 13. There, too, the overall trend in n_{NO} shown in the top row reflects contributions of the first term in eq 12. The large fluctuations in the Pt(321) rate order result primarily from ordering near the 0.6 and 0.8 ML ground states that make both the number and energies of sites vary in nonsmooth ways. Whether such variations persist or could be resolved under experimental conditions is unclear. What is clear is that the rate order should not be used to infer information about the variations in total numbers of sites (second term in eq 12) because its contribution to the rate orders is overwhelmed by the strong coverage dependence in oxygen binding energies.

The apparent activation energy has more contributions:

$$E_{app}^{\ddagger} = -k_B\left(\frac{\partial \ln A}{\partial \frac{1}{T}}\right)_{P_{O_2}} + \bar{E}_a + \frac{1}{T}\left(\frac{\partial \bar{E}_a}{\partial \frac{1}{T}}\right)_{\mu_O} - k_B\left(\frac{\partial \ln\left(\sum_i^{\text{rxn sites}} \frac{\tilde{s}_i}{\tilde{s}_{max}}\right)}{\partial \frac{1}{T}}\right)_{\mu_O} + n_{NO}\,\Delta H_{rxn}^{\circ}(T) \quad (13)$$

The temperature dependence of the prefactor, A, is on the order of $(1/2)k_BT$ (0.025 eV at 600 K). Figure 16a plots $\bar{E}_a$ and $\sum_i \tilde{s}_i/\tilde{s}_{max}$ vs $1/T$ at several O chemical potentials in the range of experimental interest for both the Pt(111) and Pt(321) models. Both quantities have little temperature dependence, and thus, the third and fourth terms in eq 13 contribute little to the apparent

DOI: 10.1021/cs501783q
ACS Catal. 2015, 5, 1087−1099

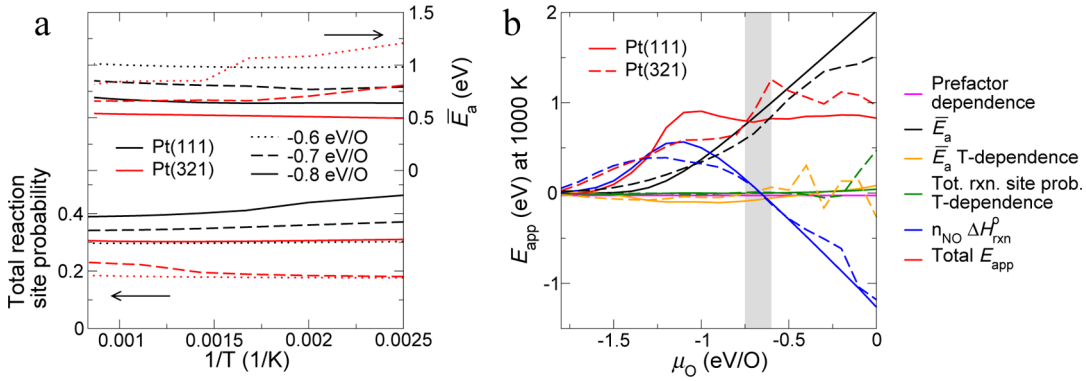

Figure 16. (a) Site-averaged activation energy, $\overline{E}_a$, and total reaction sites vs $1/T$ at $\mu_O = -0.6$, -0.7, and -0.8 eV/O. (b) Apparent activation energy contributions from each term in eq 13 vs simulation chemical potential. Solid lines, Pt(111); dashed lines, Pt(321). Results shown at 1000 K to reduce large fluctuations present at lower temperatures. Gray shaded region indicates experimental NO oxidation conditions with NO_2/NO ratio ~ 1.

activation energies. This observation is consistent with the fact that the GCMC results for the distribution of reaction sites are more sensitive to μ_O than they are to temperature. Rather, $E^{\ddagger}_{app}$ is dominated by $\overline{E}_a$ and the final term, which involves the apparent rate order and enthalpy of reaction 1. Figure 16b shows the values of these contributions to $E^{\ddagger}_{app}$ vs μ_O at 1000 K. On both surfaces, $\overline{E}_a$ increases steadily while the enthalpy term increases initially to a maximum and then decreases such that these terms vary in opposite directions in the region of experimental observation and $E^{\ddagger}_{app}$ is nearly constant. Differences in $E^{\ddagger}_{app}$ between Pt(111) and Pt(321) appear largely due to the differences in NO rate order, which influences the final term in eq 13 (blue lines in Figure 16).

4. DISCUSSION

As shown in Figure 14, the coverage-dependent NO oxidation models presented here nicely reproduce the general features of the observed NO oxidation kinetics on Pt(111) and Pt(321). The computed NO oxidation rates on the two surfaces are similar over the entire range of conditions, although deviations are present in some regions of Figure 12 (low temperatures, near strongly ordered ground state structures). These results agree qualitatively with the experimental observation that NO oxidation rates are the same to within a factor of 2 on Pt(111) and Pt(321).[14]

Coverage-dependent oxygen binding is an inextricable element of catalytic NO oxidation over metals. In the low-coverage limit, O binding on either Pt(111) or Pt(321) is so strong as to prevent reaction 1 from proceeding. It is the passivation of the metal surfaces with increasing oxygen coverage that brings binding energies into a region that allows reaction to go forward. While this coverage dependence can be captured approximately in more empirical models[15,23−25] on Pt(111), the CE approach robustly captures this coverage dependence both on the simple (111) surface and the structurally more complicated (321). At equivalent chemical potential and temperature, adsorbate coverage is roughly 50% greater on (321) than (111), and both surfaces can dissociate O_2 at useful rates at these coverages. Other late transition metals exhibit this same O coverage dependence, but not all can achieve binding energies and dissociation sites in the reaction conditions necessary for NO oxidation.[29]

That the NO oxidation reaction is structure-insensitive over Pt indicates that the differences in surface structure, coverage-dependence in binding energies, and even in BEP relationships interact in a way to yield similar net rates under the conditions probed in available experiments. This similarity is evident in the similar site-averaged activation energies. Rate derivatives interrogate reactivity more sensitively, and here, differences are seen both in experiment and in the calculations reported here. On the basis of the analysis of rate derivatives summarized in Figures 15 and 16, we conclude that the observed structure insensitivity is a result of similar site-averaged activation energies and their derivatives in both systems over the conditions explored in experiments. Model results in Figures 15 and 16 predict that structure sensitivity will reveal itself at chemical potentials (NO_2/NO ratios) outside the experimental conditions.

The kinetic model used here includes a number of simplifying assumptions. NO coverage is taken to be negligibly small, an assumption that will break down as P_{NO_2}/P_{NO} becomes small. Test calculations show that inclusion of NO adsorption yields the same total coverage and reaction rates.[23] Further, reaction 1 is assumed to be much more rapid than reaction 2, an assumption that is supported both by calculations[23,28] and experiments.[12] Further, the "reaction site" model assumes that O_2 dissociation occurs at certain sites and that differences in rates at those sites depend only on differences in activation energies through a BEP. More complicated assumptions, including more general definitions of reaction sites, site-specific sticking coefficients, and even site-specific dissociation barriers could be included within the framework described here. That the model as used recovers semiquantitatively the behavior in Figure 14 gives some measure of confidence that the model assumptions are reasonable. Further, these chemical simplifications aid in the interpretation of the results in terms of simple physical processes, something that becomes increasingly difficult with more complicated models. For instance, by analysis, we show that NO and NO_2 rate orders depend much more sensitively on the coverage-dependent binding energies than they do on statistical changes in the number of available reaction sites with O coverage and that inference of reaction mechanism from rate orders is not justified.

It is worth commenting further on the challenges in creating a BEP applicable to high coverage on the lower symmetry surface. The O_2 dissociation pathways on Pt(321)−O present numerous local minima, and choice of transition and final state energies is somewhat arbitrary. Our work on O_2 dissociation on Pt(111) highlights the fact that BEP correlations can depend on the details of the chosen reaction pathway.[31] Others have also demonstrated that the linearity of the BEP relationship depends largely on the structural similarity of each reaction pathway.[42]

DOI: 10.1021/cs501783q
ACS Catal. 2015, 5, 1087−1099

Although we can only present bounds on an appropriate BEP, our proposed BEP relationship agrees generally with literature BEPs for stepped surfaces. Quantitative discrepancies between the model and experimental results can certainly be attributed in part to these issues.

The general insensitivity of predicted NO oxidation rates to catalyst structure shown in this work implies that the experimentally observed structure sensitivity in NO oxidation on supported Pt is most likely due to differences in stability of the large and small particles. Pt is unstable to formation of bulk oxides under representative NO oxidation conditions. However, reorganization and oxidation is likely easier in the presence of steps and kinks that could serve as nucleation sites for surface oxide precursors. This hypothesis is further supported by DFT calculations[32] that show that Pt(321) surface atoms are more mobile than their Pt(111) counterparts.

5. CONCLUSIONS

Catalytic NO oxidation to NO_2 over Pt occurs at sufficiently high O coverages for both reactions 1 and 2 to have appreciable rates. Given this strong coverage sensitivity, one might expect the reaction to exhibit a strong structure sensitivity. Here, we use cluster expansion models of O adsorption and O_2 dissociation BEPs within a reaction site framework to compare NO oxidation kinetics on Pt(111) and Pt(321). We find that although the surfaces attain different coverages and are described by different BEPs, absolute rates and apparent kinetics are similar within the range of published experimental conditions. We show that coverage-dependent binding energies dominate both the rates and rate derivatives. Structural differences do lead to different O_2 dissociation energetics, ordering tendencies, and statistical availability of reaction sites under the same reaction conditions. These differences tend to counteract each other to yield the observed structure insensitivity. The models indicate that differences between the two facets would become evident at conditions outside those explored in the laboratory. Structure sensitivity observed on supported particles is more likely a consequence of different oxidation tendencies rather than differences in absolute rates as a function of size.

The reaction site approach is particularly useful when a single reaction is rate controlling and is sensitive to reaction conditions. The model form lends itself to analysis that illuminates the physical phenomena that contribute to observed kinetics. The model does not depend on mean-field approximations and avoids more time-consuming and more highly parametrized kinetic Monte Carlo calculations. Further, it provides site-averaged properties that could be used to parametrize simpler models, and in principle can be extended to more complicated reaction networks. Further, the approach can be applied to other problems, as has been recently demonstrated for O_2 temperature-programmed desorption from Pt(111).[43]

■ ASSOCIATED CONTENT

Supporting Information

The following file is available free of charge on the ACS Publications website at DOI: 10.1021/cs501783q

Additional details of NEB calculations, BEP correlation development, definition of the reaction site model, and rate order and apparent activation energy derivations (PDF)

■ AUTHOR INFORMATION

Corresponding Author

*E-mail: wschneider@nd.edu.

Notes

The authors declare no competing financial interest.

■ ACKNOWLEDGMENTS

We acknowledge funding from the Department of Energy, Basic Energy Sciences grant DE-FG02-06ER15839. We also appreciate computational resources from the University of Notre Dame Center for Research Computing as well as several years of collaboration, groundwork, and feedback provided by Prof. Fabio Ribeiro, Prof. Jean-Sabin McEwen, Prof. Chao Wu, Dr. David Schmidt, and Dr. Kurt Frey.

■ REFERENCES

(1) Shelef, M.; McCabe, R. *Catal. Today* **2000**, *62*, 35−50.
(2) Mulla, S. S.; Chen, N.; Cumaranatunge, L.; Blau, G. E.; Zemlyanov, D. Y.; Delgass, W. N.; Epling, W. S.; Ribeiro, F. H. *J. Catal.* **2006**, *241*, 389−399.
(3) Salasc, S.; Skoglundh, M.; Fridell, E. *Appl. Catal., B* **2002**, *36*, 145−160.
(4) Epling, W. S.; Campbell, L. E.; Yezerets, A.; Currier, N. W.; Parks, J. E. *Catal. Rev.* **2004**, *46*, 163−245.
(5) Despres, J.; Elsener, M.; Koebel, M.; Krocher, O.; Schnyder, B.; Wokaun, A. *Appl. Catal., B* **2004**, *50*, 73−82.
(6) Hamada, H.; Kintaichi, Y.; Inaba, M.; Tabata, M.; Yoshinari, T.; Tsuchida, H. *Catal. Today* **1996**, *29*, 53−57.
(7) Ohtsuka, H. *Appl. Catal., B* **2001**, *33*, 325−333.
(8) Cooper, B. J.; Jung, H. J.; Thoss, J. E. Treatment of diesel exhaust gases. 1990; US Patent 4,902,487.
(9) Mulla, S.; Chen, N.; Delgass, W.; Epling, W.; Ribeiro, F. *Catal. Lett.* **2005**, *100*, 267−270.
(10) Smeltz, A. D.; Getman, R. B.; Schneider, W. F.; Ribeiro, F. H. *Catal. Today* **2008**, *136*, 84−92.
(11) Weiss, B. M.; Iglesia, E. *J. Phys. Chem. C* **2009**, *113*, 13331−13340.
(12) Getman, R. B.; Schneider, W. F.; Smeltz, A. D.; Delgass, W. N.; Ribeiro, F. H. *Phys. Rev. Lett.* **2009**, *102*, 076101.
(13) Bhatia, D.; McCabe, R. W.; Harold, M. P.; Balakotaiah, V. *J. Catal.* **2009**, *266*, 106−119.
(14) Smeltz, A. D.; Delgass, W. N.; Ribeiro, F. H. *Langmuir* **2010**, *26*, 16578−16588.
(15) Mei, D.; Du, J.; Neurock, M. *Ind. Eng. Chem. Res.* **2010**, *49*, 10364−10373.
(16) Bray, J. M.; Schneider, W. F. *Langmuir* **2011**, *27*, 8177−8186.
(17) van Hardeveld, R.; Hartog, F. *Surf. Sci.* **1969**, *15*, 189−230.
(18) Hauptmann, W.; Votsmeier, M.; Gieshoff, J.; Vlachos, D.; Drochner, A.; Vogel, H. *Top. Catal.* **2009**, *52*, 1925−1928.
(19) Evans, M. G.; Polanyi, M. *T. Faraday Soc.* **1938**, *34*, 11−24.
(20) Bligaard, T.; Nørskov, J. K.; Dahl, S.; Matthiesen, J.; Christensen, C. H.; Sehested, J. *J. Catal.* **2004**, *224*, 206−217.
(21) Nørskov, J. K.; Bligaard, T.; Logadottir, A.; Bahn, S.; Hansen, L. B.; Bollinger, M.; Bengaard, H.; Hammer, B.; Sljivancanin, Z.; Mavrikakis, M.; Xu, Y.; Dahl, S.; Jacobsen, C. J. H. *J. Catal.* **2002**, *209*, 275−278.
(22) Nørskov, J. K.; Bligaard, T.; Hvolbaek, B.; Abild-Pedersen, F.; Chorkendorff, I.; Christensen, C. H. *Chem. Soc. Rev.* **2008**, *37*, 2163−2171.
(23) Getman, R. B.; Schneider, W. F. *ChemCatChem* **2010**, *2*, 1450−1460.
(24) Mei, D.; Ge, Q.; Neurock, M.; Kieken, L.; Lerou, J. *Mol. Phys.* **2004**, *102*, 361−369.
(25) Ovesson, S.; Lundqvist, B. I.; Schneider, W. F.; Bogicevic, A. *Phys. Rev. B* **2005**, *71*, 115406.
(26) Schmidt, D. J.; Chen, W.; Wolverton, C.; Schneider, W. F. *J. Chem. Theory Comput.* **2012**, *8*, 264−273.

DOI: 10.1021/cs501783q
ACS Catal. 2015, 5, 1087−1099

(27) Wu, C.; Schmidt, D.; Wolverton, C.; Schneider, W. *J. Catal.* **2012**, *286*, 88−94.
(28) Nielsen, J.; d 'Avezac, M.; Hetherington, J.; Stamatakis, M. *J. Chem. Phys.* **2013**, *139*, 224706.
(29) Frey, K.; Schmidt, D. J.; Wolverton, C.; Schneider, W. F. *Catal. Sci. Technol.* **2014**, *4*, 4356−4365.
(30) Getman, R. B.; Xu, Y.; Schneider, W. F. *J. Phys. Chem. C* **2008**, *112*, 9559−9572.
(31) McEwen, J.-S.; Bray, J. M.; Wu, C.; Schneider, W. F. *Phys. Chem. Chem. Phys.* **2012**, *14*, 16677−16685.
(32) Bray, J. M.; Smith, J. L.; Schneider, W. F. *Top. Catal.* **2014**, *57*, 89−105.
(33) Kresse, G.; Furthmüller, J. *Phys. Rev. B* **1996**, *54*, 11169−11186.
(34) Perdew, J. P.; Wang, Y. *Phys. Rev. B* **1992**, *45*, 13244−13249.
(35) Blöchl, P. E. *Phys. Rev. B* **1994**, *50*, 17953−17979.
(36) Kresse, G.; Joubert, D. *Phys. Rev. B* **1999**, *59*, 1758−1775.
(37) Henkelman, G.; Uberuaga, B. P.; Jónsson, H. *J. Chem. Phys.* **2000**, *113*, 9901−9904.
(38) McClellan, M. R.; McFeely, F. R.; Gland, J. L. *Surf. Sci.* **1983**, *124*, 188−208.
(39) Bray, J. M.; Schneider, W. F. In *Computational Catalysis*; Janik, M., Asthagiri, A., Eds.; The Royal Society of Chemistry: London, 2014; pp 59−115.
(40) Wang, S.; Temel, B.; Shen, J.; Jones, G.; Grabow, L. C.; Studt, F.; Bligaard, T.; Abild-Pedersen, F.; Christensen, C. H.; Nørskov, J. K. *Catal. Lett.* **2011**, *141*, 370−373.
(41) Logadottir, A.; Rod, T.; Nørskov, J.; Hammer, B.; Dahl, S.; Jacobsen, C. *J. Catal.* **2001**, *197*, 229−231.
(42) Munter, T. R.; Bligaard, T.; Christensen, C. H.; Nørskov, J. K. *Phys. Chem. Chem. Phys.* **2008**, *10*, 5202−5206.
(43) Bray, J. M.; Skavdahl, I. J.; McEwen, J.-S.; Schneider, W. F. *Surf. Sci.* **2014**, *622*, L1−L6.

DOI: 10.1021/cs501783q
ACS Catal. 2015, 5, 1087−1099